Title

Surface molecular pump enables ultrahigh catalyst activity.

Journal

Science Advances, 10(36)

Authors

Huang, Jin
Peng, Bosi
Zhu, Cheng
et al.

Publication Date

2024-09-06

DOI

10.1126/sciadv.ado3942

Peer reviewed

MATERIALS SCIENCE

Surface molecular pump enables ultrahigh catalyst activity

Jin Huang[1]†, Bosi Peng[1,2]†, Cheng Zhu[3]†, Mingjie Xu[4,5], Yang Liu[1], Zeyan Liu[1], Jingxuan Zhou[1], Sibo Wang[2], Xiangfeng Duan[2,6], Hendrik Heinz[3,7]*, Yu Huang[1,6]*

The performance of electrocatalysts is critical for renewable energy technologies. While the electrocatalytic activity can be modulated through structural and compositional engineering following the Sabatier principle, the insufficiently explored catalyst-electrolyte interface is promising to promote microkinetic processes such as physisorption and desorption. By combining experimental designs and molecular dynamics simulations with explicit solvent in high accuracy, we demonstrated that dimethylformamide can work as an effective surface molecular pump to facilitate the entrapment of oxygen and outflux of water. Dimethylformamide disrupts the interfacial network of hydrogen bonds, leading to enhanced activity of the oxygen reduction reaction by a factor of 2 to 3. This strategy works generally for platinum-alloy catalysts, and we introduce an optimal model PtCuNi catalyst with an unprecedented specific activity of 21.8 ± 2.1 mA/cm^2 at 0.9 V versus the reversible hydrogen electrode, nearly double the previous record, and an ultrahigh mass activity of 10.7 ± 1.1 A/mg$_{Pt}$.

INTRODUCTION

Improvements in performance of costly catalysts (e.g., platinum) are critical for the storage and conversion of renewable clean energy (*1*). Intensive efforts have been devoted to searching for catalysts with higher catalytic activity (*2*–*5*) and longer-term stability (*6*, *7*). A generally adopted strategy is through the strain effect (*2*, *8*) or the ligand effect (*3*, *9*) to achieve an optimal binding energy between catalyst surface and reaction species, which can lower the overpotential of the reaction and enhance the activity. Despite considerable progress made so far, further enhancement is required. Meanwhile, such guidance has been largely motivated by theoretical considerations in vacuum, while microkinetics at the catalyst-electrolyte interface was rarely taken into quantitative consideration. A long-standing issue for many electrochemical reactions is the insufficient reactant supply at the catalyst surface. For example, the low oxygen solubility (2.56×10^{-4} M) in 0.1 M $HClO_4$ and small equilibrium constants for initial physisorption (*10*, *11*) impede the already sluggish oxygen reduction reaction (ORR) kinetics. Quantitative understanding of such solid-electrolyte interfaces with gases and other reactants can be gained through simulations with the INTERFACE force field (IFF) (*12*) which reaches a high accuracy of ~0.03 kcal/mol (*11*, *13*). Advances to address this challenge in experiments have been made through the development of a high oxygen permeability ionomer (*14*) or hydrophobic ionic liquids with a higher bulk O_2 solubility (ca. 2.4 times compared to that in 0.1 M $HClO_4$) (*15*–*17*) with success, although at a higher developmental or material cost. In parallel, timely removal of reactant water is of equal importance to accelerate the reaction (*18*, *19*), following Le Chatelier's principle. Recently, the addition of cations (*20*), pyridine (*21*), melamine (*22*), melamine-formaldehyde polymer (*23*), and tetrahexylammonium cations (*24*) in the electrolyte has been shown to effectively improve the ORR kinetics of pure Pt. These studies attributed the activity enhancement to the destabilization or weakening of OH_{ad} adsorption on the Pt surface, which promotes the ORR activity following the Sabatier principle, whereby final protonation could be the rate-determining step. However, such ligand enhancement mechanisms remain elusive to verify, given the weak attraction of oxygen to Pt in aqueous solution (*11*), and more in-depth analysis is necessary.

Herein, we demonstrated that a ligand can act as a surface molecular pump to substantially accelerate reactant supply and product removal in ORR (Fig. 1) (*25*). We propose a concept of "molecular pump" to illustrate the net effect of dimethylformamide (DMF) surface modification, showing that DMF pulls in more O_2 through increased physisorption of O_2 on the surface and releases more H_2O per unit time (decreased H_2O adsorption time). The local Pt-O_2 concentration, c_{Pt-O2}, could be approximately doubled and the surface molecular pump allows for reduced surface water concentration and retention time, leading to faster outflux of water. Together, the surface molecular pump can further enhance the specific activity (SA) of electrocatalytic reactions (e.g., ORR). Our experimental studies revealed that adsorbed DMF molecules, as a surface molecular pump, can effectively improve the SA of Pt/C by twofold in 0.1 M $HClO_4$ electrolyte. Our molecular dynamics (MD) simulations with the IFF suggest that physisorption of DMF on the Pt surface can accelerate O_2 transport from the electrolyte toward the Pt surface, lower the oxygen Gibbs physisorption energy and prolong the oxygen contact time. DMF thus greatly affects the physisorption behavior of O_2 toward Pt, which was recently related to the overall chemical reaction process (*11*). Reactions require milliseconds at the nanometer scale to occur and therefore strongly depend on preceding physisorption equilibria (Fig. 1). Because of a much shorter timescale of nanoseconds and low binding free energies of O_2 below −0.6 kcal/mol (−0.025 eV), physisorption has an immense effect on the interfacial microenvironment, which

[1]Department of Materials Science and Engineering, University of California, Los Angeles, CA 90095, USA. [2]Department of Chemistry and Biochemistry, University of California, Los Angeles, CA 90095, USA. [3]Department of Chemical and Biological Engineering, University of Colorado Boulder, Boulder, CO 80309, USA. [4]Irvine Materials Research Institute, University of California, Irvine, CA 92697, USA. [5]Department of Materials Science, University of California, Irvine, CA 92697, USA. [6]California NanoSystems Institute, University of California, Los Angeles, CA 90095, USA. [7]Materials Science and Engineering Program, University of Colorado Boulder, Boulder, CO 80309, USA.
*Corresponding author. Email: yhuang@seas.ucla.edu (Y.H.); hendrik.heinz@colorado.edu (H.H.)
†These authors contributed equally to this work.

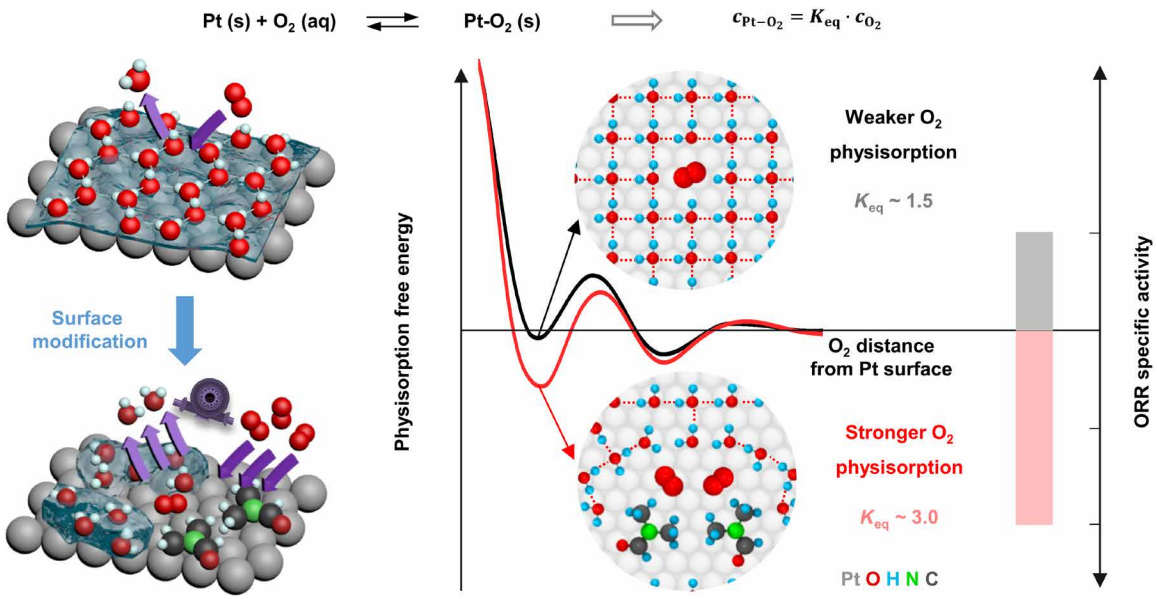

Fig. 1. Schematic illustration of the boosted ORR kinetics by surface modification of Pt. The application of DMF as an oxygen trap and a surface molecular pump can facilitate higher interfacial oxygen concentration (c_{Pt-O2}) and lower interfacial water concentration by breaking the network of hydrogen bonds in water adlayers on the Pt surface (left). The surface molecular pump lowers the physisorption free energy of O_2 on the surface and shifts the physisorption equilibrium constant toward higher ORR specific activity (right, length of light red bar). The specific activity is shown in arbitrary units for simplicity and a color legend for the atoms is included on the lower right.

directly correlates with the ORR kinetic current (*11*, *26*). Our MD simulations show that DMF physisorption on the Pt surface leads to increased interfacial O_2 concentration and reduced water concentration on the Pt surface, which collectively boosts the ORR activity by way of Le Chatelier's principle (Fig. 1). We further applied this approach to a model Pt-alloy catalyst (PtCuNi), achieving an unprecedented ORR SA of 21.8 ± 2.1 mA/cm^2 at 0.9 V versus the reversible hydrogen electrode (RHE), which nearly doubles the previously reported record in the literature (*27*), leading to an ultrahigh mass activity (MA) of 10.7 ± 1.1 A/mg$_{Pt}$.

RESULTS

Surface modification of commercial Pt/C catalysts

We first used Pt/C catalysts [40 weight % (wt %) Pt, HiSPEC 4000, Johnson Matthey] as a model system to explore the effect of surface molecular pumps. DMF was chosen as the surface ligand due to its stability in a wide potential window (*28*) and the strong physisorption of amides in close contact following a soft epitaxial pattern, which has been previously described (*29*). We treated the Pt/C catalyst in a pure DMF solution at 120°C for a varied period of time to allow gradual molecular adsorption on the surface (see the Supplementary Materials). We chose the elevated temperature because it can equilibrate an even distribution of DMF on the catalyst surface faster than at room temperature and enhance the sampling of surface coverage with DMF over a wide range of values. Cyclic voltammetry (CV) revealed that the Pt/C catalysts exhibited an initial electrochemically active surface area (ECSA) (based on hydrogen underpotential deposition, H_{upd}) of 51.6 ± 1.5 m^2/g$_{Pt}$, which decreased to 21.8 ± 0.2 m^2/g$_{Pt}$ after 48 hours of modification evidenced by a decreased H_{upd} area (Fig. 2A). The size of Pt catalysts and carbon support did not show noticeable size changes upon surface modification (figs. S1 and S2), indicating that the reduction of ECSA upon treatment can be attributed to the blocking of available Pt surface sites with increasing DMF surface coverage (defined as the reduced ECSA: the decreased H_{upd} region normalized by the original H_{upd} region of the catalyst, Fig. 2B). Our x-ray photoelectron spectroscopy (XPS) studies (fig. S3) revealed that the presence of N-species increased with longer modification time, indicating an increased amount of adsorbed DMF, which is consistent with the decreased ECSA (Fig. 2B). We did not observe apparent shift in the XPS peak position for both $4f_{7/2}$ and $4f_{5/2}$ peaks, suggesting that surface-adsorbed ligands do not induce notable electronic effects on Pt (fig. S3B).

We further evaluated the ORR activities of Pt/C catalysts using the linear sweep voltammetry (LSV) method (Fig. 2C). The SA of Pt/C catalysts increased from 0.48 ± 0.06 to 0.89 ± 0.04 mA/cm^2 after 24 hours of modification (surface coverage of 37.1%) and then decreased to 0.55 ± 0.02 mA/cm^2 after 48 hours of modification (surface coverage of 58.0%) (Fig. 2D). Accordingly, the MA of Pt/C catalyst increased from 0.23 ± 0.03 to 0.28 ± 0.03 A/mg$_{Pt}$ after 24 hours of modification (Fig. 2D). The electrochemical impedance spectroscopy did not show the ohmic resistance change for the catalyst before and after surface modification (fig. S4). We also used DMF to treat Pt disk electrode and found similar activity enhancement. In particular, we dropped 10 μl of 80°C DMF on a 5-mm-diameter Pt disk electrode and dried it in an 80°C oven. Then, we used ethanol to wash away residual DMF. Similarly, the CV curves showed a 22% areal decrease at the hydrogen underpotential region upon DMF treatment (fig. S5A). The half-wave potential of the surface-treated Pt disk is 0.818 V (vs. RHE), which is 44 mV larger than that of the untreated Pt disk (0.774 V) (fig. S5B). The SA of the surface-treated Pt disk is 0.53 mA/cm^2 (0.9 V versus RHE), which is 3.6 times higher than that of the untreated Pt disk (0.15 mA/

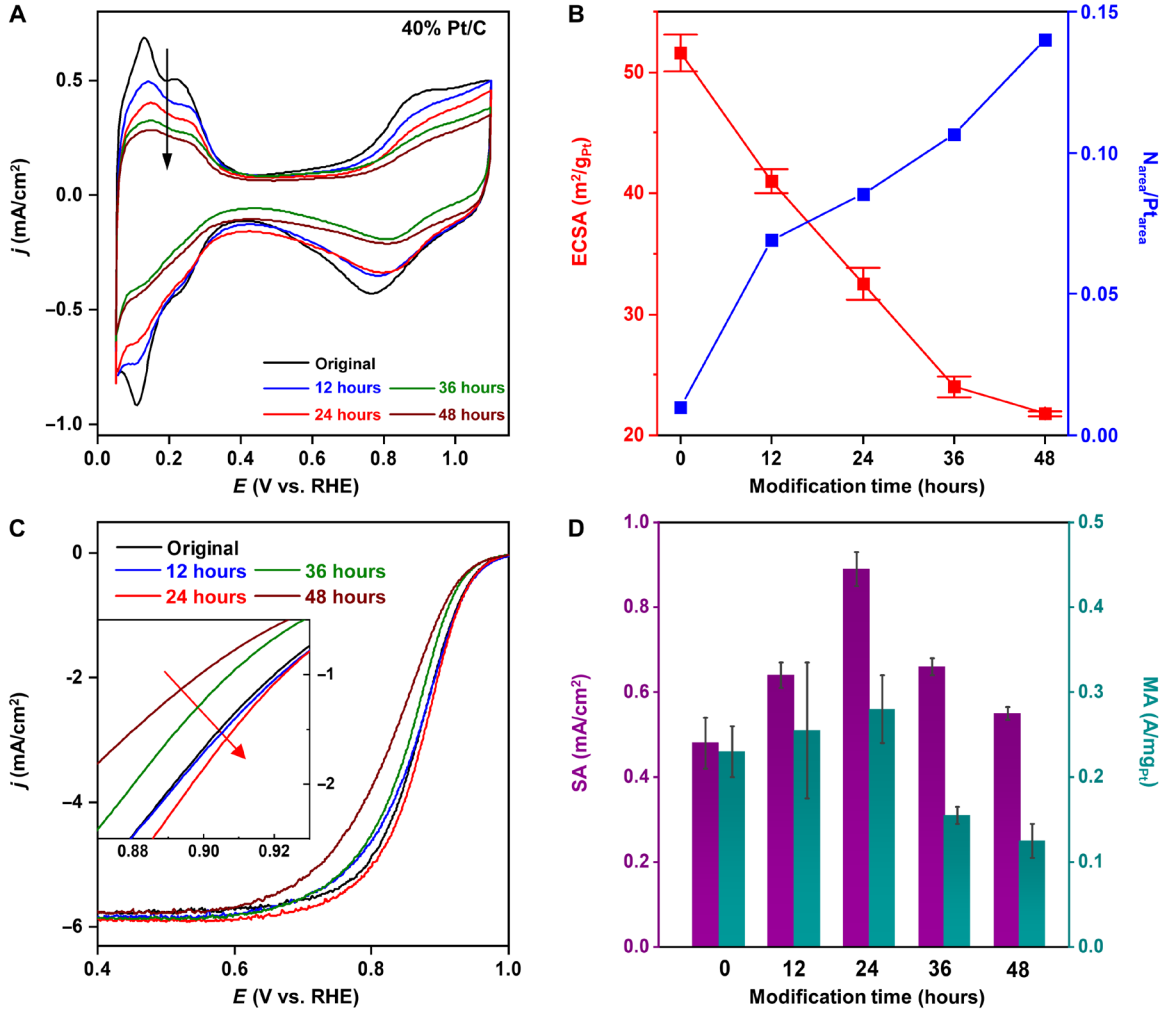

Fig. 2. Electrochemical measurements in 0.1 M $HClO_4$ electrolyte of the 40% Pt/C catalysts modified with DMF at different treatment times. (**A**) CV curves of Pt/C catalysts at the original stage (black) and after 12 hours (blue), 24 hours (red), 36 hours (green), and 48 hours (wine) of modification time. (**B**) ECSA and N/Pt ratio obtained from XPS peak integration as a function of modification time. (**C**) ORR LSV curves of Pt/C catalysts at the original stage (black) and after 12 hours (blue), 24 hours (red), 36 hours (green), and 48 hours (wine) of modification time. The inset of (C) is the enlarged potential window. (**D**) The evolution of SA (purple, left *y* axis) and MA (olive, right *y* axis) with modification time. The SAs of different stages: 0.48 ± 0.06 mA/cm^2 (0 hours), 0.64 ± 0.03 mA/cm^2 (12 hours), 0.89 ± 0.04 mA/cm^2 (24 hours), 0.66 ± 0.02 mA/cm^2 (36 hours), and 0.55 ± 0.02 mA/cm^2 (48 hours). The MAs of different stages: 0.23 ± 0.03 A/mg (0 hours), 0.26 ± 0.08 A/mg (12 hours), 0.28 ± 0.04 A/mg (24 hours), 0.16 ± 0.01 A/mg (36 hours), and 0.13 ± 0.02 A/mg (48 hours).

cm^2) (fig. S5C). These intriguing enhancements of both SAs and MAs motivated us to conduct multi-scale computational studies to understand the role of DMF in modulating the ORR activity at catalyst-electrolyte interfaces.

MD simulations of kinetics at catalyst-electrolyte interfaces

We carried out MD simulations with the IFF (*12*) (see Supplementary Materials for simulation details) on a representative Pt(111) slab in a 0.1 M $HClO_4$ electrolyte including explicit solvent molecules and ions to compare the dynamics and local concentration of O_2 and H_2O at different DMF surface coverages from 0 to 100% over 50-ns timescales (fig. S6). IFF MD simulations for catalyst-electrolyte interfaces were earlier shown to be of high reliability and efficient, suitable for analyzing realistically sized nanostructures and their dynamics (*11*). Without the addition of DMF (Fig. 3A), adsorbed O_2 molecules on the Pt(111) surface were surrounded by approximately seven to eight H_2O molecules, forming a dense network of hydrogen bonds (blue circles). The circles with decreasing blue segments indicate that the number of H_2O molecules surrounding the O_2 molecules adsorbed onto Pt considerably decreased for higher coverage with DMF molecules (Fig. 3, A to C). DMF molecules preferred to be flatly adsorbed on the Pt(111) surface with a physisorption energy of −17.3 ± 2 kcal/mol in an aqueous solution (Fig. 3, B and C, and figs. S6, B to E, and S7A), and −37.5 ± 1 kcal/mol in vacuum (fig. S7D). Both energy differences support the strong binding of DMF to Pt(111) and the permanent replacement of H_2O molecules on the surface, which have a lower adsorption energy of −6.6 ± 1 kcal/mol on the Pt(111) surface in vacuum and create the characteristic adlayer structure of H_2O in solution. It is unlikely that DMF is removed from the surface.

When approaching the catalyst surface to gain direct access to the metal, O_2 molecules have to overcome free energy barriers to

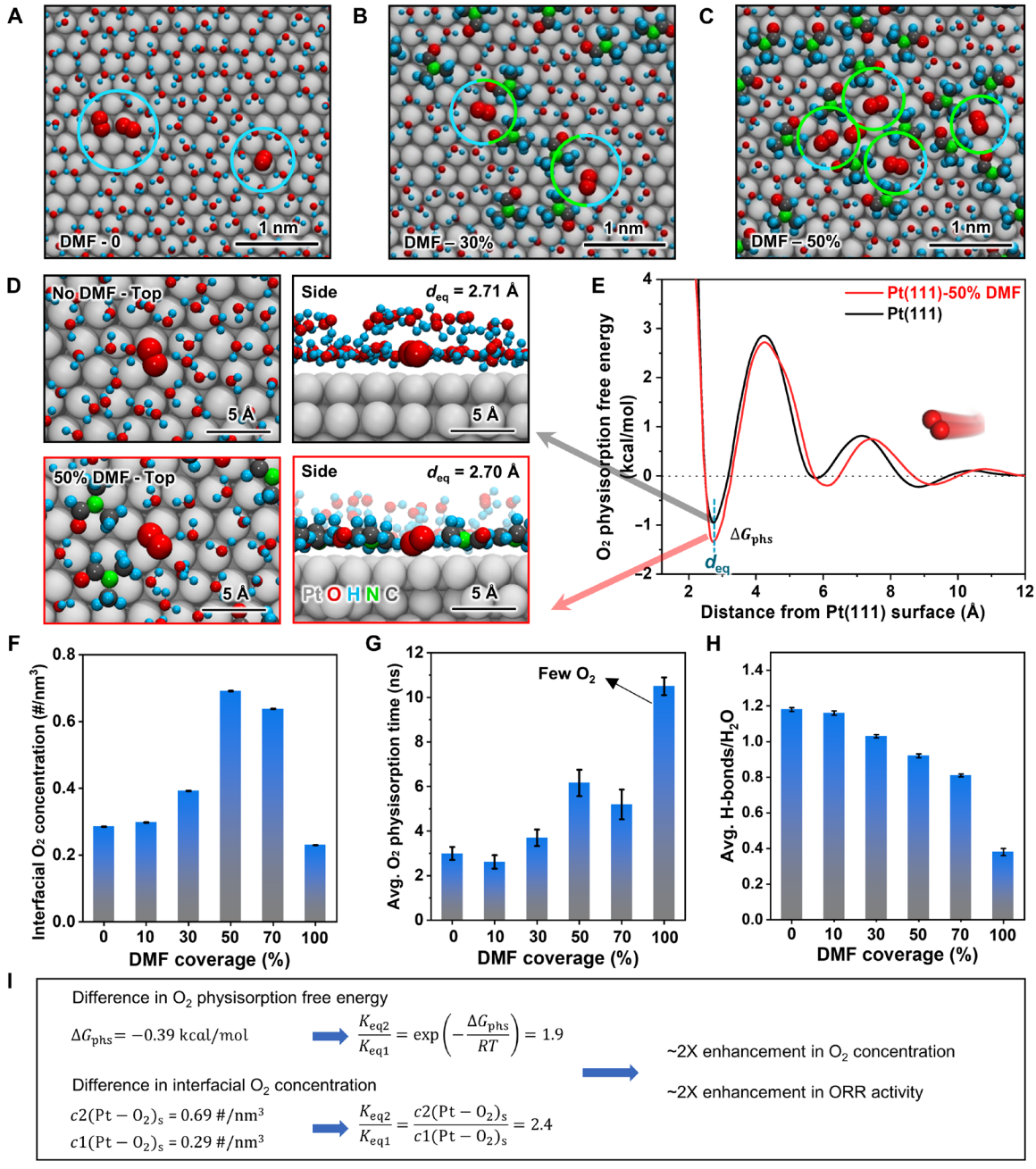

Fig. 3. Molecular structure and dynamics of the catalyst-electrolyte interface, and the effect of the DMF from IFF MD simulations. (**A** to **C**) Snapshots of the molecular conformations of O_2, water, and DMF on the Pt(111) surface at a DMF coverage of (A) 0%, (B) 30%, and (C) 50%. The circles represent the surrounding H_2O (blue) and DMF methyl groups (green) of adsorbed O_2 molecules. (**D**) Top and side views of the Pt(111) and Pt(111)–50% DMF surface, showing how DMF disrupts the water adlayer integrity and O_2 molecules are attracted by vdW interactions to both DMF and Pt. (**E**) Comparison of O_2 physisorption free energy on Pt(111) and Pt(111)–50% DMF surface from SMD simulations. d_{eq} is the equilibrium distance for O_2 contact with the Pt(111) surface. (**F**) The relationship between DMF surface coverage and interfacial O_2 concentration (number of molecules/nm^3). The cutoff of the interfacial layer was set as 0.5 nm from the Pt surface (*30*). (**G**) Average physisorption time of O_2 molecules on the Pt(111) surface (cutoff, 3.5 Å). (**H**) Average number of H-bonds per H_2O molecule on the Pt(111) surface (cutoff, 3.5 Å). (**I**) Two methods of estimating the change of equilibrium constants K_{eq} and implications for the observed relative ORR activity. The upper equations show the change in the physisorption free energy ΔG for 0 and 50% DMF coverage, and the lower equations show the change in the interfacial O_2 concentration for 0 and 50% DMF coverage. Ions in the electrolyte are hidden for clarity. Error bars represent the standard error of mean (SEM).

penetrate the hydrogen-bonded network of water molecules on the Pt surface and replace between one and two surface-bound H_2O molecules (Fig. 3, A, D, and E) (*11*). In the presence of the molecular pump DMF, O_2 molecules can more conveniently reach the Pt surface near the methyl groups of DMF molecules, enabling multiple van der Waals (vdW) interactions that increase O_2 interaction with and retention on the Pt surface (Fig. 3, B to E). The free energy barriers for physisorption are hereby small enough (<3 kcal/mol or <0.13 eV) and crossed within hundreds of picoseconds, without an effect on the statistical physisorption equilibrium beyond nanoseconds (Fig. 3E).

Thus, we analyzed the equilibrium properties such as the interfacial concentration and physisorption time of O_2 and H_2O (figs. S8 and S9). Within an interfacial layer of 0.5 nm thickness (*30*), the O_2 concentration increased from 0.29 to 0.69 nm^{-3}, i.e., by a factor of 2.4, with a corresponding increase in DMF coverage from 0 to 50%; and decreased to 0.64 nm^{-3} when DMF coverage reached 70%, then to 0.23 nm^{-3} at 100% coverage (Fig. 3F). The average physisorption time of O_2 on the Pt (111) surface was prolonged to 6.2 ns at 50% DMF coverage compared to 3.0 ns for the pure Pt(111) surface (Fig. 3G), corresponding to an increase by a factor of 2.1. The average physisorption time at 10% DMF coverage (2.6 ± 0.3 ns) is slightly lower than that at 0% DMF coverage (3.0 ± 0.3 ns), which is within the statistical uncertainty of the simulation, and a clear trend toward higher coverage is seen. At 70% DMF coverage, a fraction of O_2 molecules has much-prolonged physisorption times (>20 ns) due to vdW interactions with DMF, and 47% of O_2 molecules had barely any contact with the Pt(111) surface (fig. S8). As a result, the average O_2 physisorption time at 70% DMF coverage (5.2 ns) is shorter than that at 50% DMF coverage (6.2 ns) (Fig. 3G). Furthermore, 100% DMF coverage blocked the adsorption of O_2, leading to a markedly decreased percentage of adsorbed O_2 (fig. S8). However, DMF molecules cannot fully cover the surface due to strong packing constraints and leave adequate spaces that can still trap a few O_2 molecules (figs. S6F, S8, and S10F). The exceptional attraction of few O_2 molecules with adsorption time of more than 40 ns resulted in an anomalous large average adsorption time of 10.85 ns (averaged among adsorbed O_2 molecules) at 100% DMF coverage (Fig. 3G and fig. S8).

In addition to local oxygen entrapment by increasing the DMF coverage from 0 to 100%, the interfacial H_2O concentration decreased from 30.1 to 6.0 nm^{-3} within the 0.5-nm surface layer (fig. S9A) and the average physisorption time of H_2O declined markedly from 3.5 to 0.3 ns (fig. S9B). This change signifies that the surface molecular pump also facilitated product (water) removal, thereby speeding up the ORR rate. The average number of H-bonds per H_2O molecule within the adlayer (see the Supplementary Materials for simulation details) also showed a continuous decrease from 1.18 to 0.38 with increasing DMF coverage, indicating a notable reduction of the H-bond network due to DMF functioning as a molecular pump (Fig. 3H). The analysis of hydrogen bonds assumes a maximum O(H) ··· O distance of 3.5 Å and a maximum deviation of 30° from the linear (H)O—H ··· O(H_2) angle (*31*). The average number of H-bonds per water molecule was calculated by dividing the total number of formed H-bonds by the total number of H_2O molecules in the adlayer. In addition, the configuration of the adlayer network of water (blue shade in fig. S10) shows a sparser and increasingly incomplete pattern when the Pt(111) surface coverage by DMF increases from 0 to 100%, providing more space near the molecular pump DMF for O_2 adsorption (pale violet red shade). Our surface wettability test results showed that the contact angle increased with increasing treatment time for both Pt/C and PtCuNi catalysts (fig. S11), which indicated that the catalyst surface became more hydrophobic. This finding is consistent with our hypothesis that a modified catalyst surface facilitates water removal, thus favorably shifting reaction kinetics and improving ORR. We also investigated the interfacial H_3O^+ concentration in MD simulations (fig. S12). The interfacial H_3O^+ concentration gradually decreases from 0.55 to 0.17 nm^{-3} with an increase of DMF coverage, which indicates a slower proton transport process due to the DMF attachment. It is worth noting that the interfacial H_3O^+ concentration (0.49 nm^{-3}) only declined by 10% at 30% DMF coverage. However, the interfacial H_3O^+ concentration substantially decreased by 35% when DMF coverage reached 50%. In the experiments, we found that both Pt/C and PtCuNi catalysts first showed an activity increase and then an activity decrease. Our results indicate that the change of O_2 physisorption dynamics is the dominant factor in enhanced ORR activity. Another possible factor for the activity decrease could be reduced hydronium conduction; however, we do not expect that the proton-electron transfer process will be strongly influenced while the DMF surface coverage is less than 50%, or even somewhat higher.

To confirm the more favorable O_2-DMF configurations compared to O_2-H_2O configurations near the Pt surface, we further analyzed the stabilization energy (IFF-based simulations) of small clusters consisting of Pt, DMF, H_2O, and O_2, which represent the local environment of molecular pumps at the catalyst-electrolyte interface (fig. S13, A and B). The simulations with IFF have a unique accuracy of better than 0.03 kcal/mol (*13*) and the results corroborate that an increasing number of DMF molecules in the cluster increase the oxygen stabilization energy (fig. S13C). Hereby, coordination of O_2 with one DMF "pump" molecule replaces approximately two H_2O molecules and increases the stabilization energy by −0.24 ± 0.02 kcal/mol (fig. S13D). Therefore, DMF stabilizes O_2 physisorption on Pt and, at the same time, destabilizes H_2O physisorption, which leads to a higher interfacial O_2 concentration and lower interfacial H_2O concentration, creating a surface molecular pump that accelerates the ORR kinetics (*32*).

In particular, the MD simulations of Pt(111) with 50% DMF (Fig. 3, D and E) showed the highest interfacial O_2 concentration (0.69 nm^{-3}) within a 0.5 nm distance from the surface (*30*) and a long O_2 physisorption time (6.2 ns), equal to a higher equilibrium concentration of O_2 on the Pt surface and leading to accelerated ORR kinetics. The expected increase in the negative physisorption free energy of O_2 in the presence of DMF is quantitatively shown by the free energy profiles of O_2 molecules using steered molecular dynamics (SMD) simulations for two control cases of 0 and 50% DMF coverage (Fig. 3, D, E, and I, and figs. S14 and S15), respectively. The simulation models consider full hydration of oxygen molecules while traveling from solution to the Pt surface, as well as changes in hydration upon proximity to ions in solution or coordination with DMF on the surface, and realistic concentrations of all present electrolytes. The distance of the O_2 molecule from the Pt surface is measured between the center of mass of an O_2 molecule and the z coordinate of surface layer Pt atoms. Hereby, 10 replicas with a slow pulling speed of 0.01 Å/ns and a total simulation time of 4 μs were used to fully sample the oxygen interactions at the interface in high accuracy (see Materials and Methods). The mobility of DMF

molecules, such as surface hopping and in-plane rotation, and simultaneous rearrangements of the networks of hydrogen-bonded water molecules notably affect the O_2 dynamics at distances <0.6 nm from the surface. The O_2 molecules ultimately adsorbed to Pt (111) in coordination with DMF molecules in all replicas of the SMD simulations, showing dynamic O_2-DMF coordination numbers, and that coordination with DMF molecules is the preferred position for O_2 adsorption (Fig. 3, B to D). These results are consistent with independent IFF-based calculations of O_2 physisorption energies to small Pt(111)/DMF/water clusters, whereby an increase in O_2 coordination number with DMF from 0 to 4 increased the net stabilization energy from 0 to −0.96 kcal/mol (fig. S13D). The global free energy minimum represents direct contact of O_2 with the Pt surface and was found at 2.72 Å distance from the Pt(111) surface atoms (d_{eq}), and the total physisorption free energy (ΔG) of O_2 was, as expected, lower at −1.34 kcal/mol for Pt(111)–50% DMF compared to −0.95 kcal/mol for pure Pt(111) in water (Fig. 3E). The gain in O_2 physisorption free energy of −0.39 kcal/mol in the presence of DMF (denoted as ΔG_{phs} in Fig. 3, E and I) is consistent with the independent IFF-based calculations of the gain in O_2 physisorption energies to small clusters (fig. S13D). Although the small cluster estimates are somewhat simplistic without entropy contributions and full water dynamics, both results affirm that DMF promotes the adsorption of O_2 near the Pt(111) surface. The peaks at ~4.2 Å represent the energy barriers associated with O_2 penetration through the network of H-bonds in the closest adlayer of H_2O molecules and the simultaneous replacement of H_2O by O_2. The maximum energy barrier for the transport of O_2 from bulk electrolyte (at infinity) to the surface is lower for the 50% DMF-modified surface. The physisorption free energy (ΔG_{phs}) is directly related to the thermodynamic equilibrium constant $\left[K_{eq} = \exp\left(-\frac{\Delta G_{phs}}{RT}\right) = \frac{c(\mathrm{Pt-O_2})_s}{c(\mathrm{O_2})_{aq}}\right]$ (Figs. 1 and 3I). Accordingly, an increase in K_{eq} by a factor of 2 using DMF can effectively increase the availability of adlayer O_2 for ORR, $c(\mathrm{Pt-O_2})_s$. Although the enhanced O_2 coverage is still low on an absolute scale, a small difference of 1 *RT* (~0.59 kcal/mol at 298.15 K) can change the coverage by approximately 2.7 times. The difference in free energy minima of ΔG_{phs} of −0.39 kcal/mol (Fig. 3E) increases the equilibrium constant K_{eq} by a factor of ~2.0 $\left[\frac{K_{eq2}}{K_{eq1}} = \exp\left(-\frac{\Delta G_{phs}}{RT}\right)\right]$, semiquantitatively matching the enhancement factor in ORR SA observed in the experiments (from 0.48 to 0.89 mA/cm^2, a factor of 1.9) (Figs. 2D and 3, F, G, and I). This enhancement is also independently validated by the interfacial O_2 concentration results (Fig. 3, F and I), where the interfacial O_2 concentration at 50% DMF coverage is 2.4 times of that on pure Pt(111), equal to an increase of the equilibrium constant K_{eq} by a factor of ~2.4 according to the definition $\left[\frac{K_{eq2}}{K_{eq1}} = \frac{c2(\mathrm{Pt-O_2})_s}{c1(\mathrm{Pt-O_2})_s}\right]$. This order of magnitude, while comparable to thermal motion, is statistically significant and critical over time like in other equilibrium and kinetic processes, such as conformation equilibria in chain molecules (*33*). The interfacial O_2 concentration begins to decrease when the DMF coverage reaches 70%, which is attributed to a substantially reduced number of available Pt surface sites for O_2 adsorption. These observations agree with our experimental results and the observation that excessive surface modification will lead to a lower activity (Fig. 2D) (*34*, *35*).

The universality of molecular pumps on catalyst surfaces

Our experimental results and MD analyses suggested that the proper surface molecular pump on Pt facilitates the influx of O_2 and outflux of water, which leads to increased O_2 surface concentration and reduced H_2O concentration, and sustainably higher ORR activity. We note that this surface molecular pump follows Le Chatelier's principle, which is fundamentally different and may work independently from strategies used in modifying the electronic structures of the catalyst surface. Therefore, we expect that such effects can work synergistically to enhance the SA of Pt-alloy catalysts beyond the limits using the Sabatier principle. To this end, we prepared the PtCuNi catalyst using a modified method reported previously (*36*) and applied the same surface modification protocol. The overall average size, composition, and elemental distribution did not show noticeable change before and after modification (figs. S16, A to E, and S17, A to E). Similar to Pt/C, the ECSA of modified PtCuNi catalysts decreased from 70 to 49 m^2/g_{Pt} after 24 hours of modification and further decreased to 36 m^2/g_{Pt} after 48 hours of modification (Fig. 4A and fig. S18A). We noted that the morphology, size, composition, and structures of the modified catalysts remained overall unchanged compared to the original PtCuNi catalysts (figs. S19, A to E, and S20, A to E), suggesting that the decreased ECSA is dominantly attributed to increased DMF coverage, which is consistent with the Pt/C model system discussed above (Fig. 2A).

We further evaluated the ORR activity of surface-modified PtCuNi catalysts (fig. S18B) and found that the optimal surface-modified PtCuNi catalysts exhibited an unprecedented high SA of 21.8 ± 2.1 mA/cm^2 and an ultrahigh MA of 10.7 ± 1.1 A/mg_{Pt} at 0.9 V versus RHE (Fig. 4A), which are ca. 2.6 times and 1.9 times those of original PtCuNi catalysts (8.2 ± 0.4 mA/cm^2 and 5.7 ± 0.3 A/mg_{Pt}) and ca. 45.4 times and 46.5 times those of Pt/C catalysts (0.48 ± 0.06 mA/cm^2 and 0.23 ± 0.03 A/mg_{Pt}). The half-wave potential of surface-modified PtCuNi is 0.952 V versus RHE, which is 19 mV higher than that of unmodified PtCuNi (0.933 V versus RHE). The SA of our surface-modified PtCuNi catalysts outperforms all current state-of-the-art catalysts and nearly doubles the SA performance of previously reported J-PtNWs (11.5 mA/cm^2) (*27*) (Fig. 4B and Table 1). We also evaluated the SA at 0.95 V versus RHE and found that the activity trend remained unchanged. The optimal surface-modified PtCuNi catalysts still showed the highest SA of 1.67 ± 0.04 mA/cm^2, which is about 2.78 times that of unmodified PtCuNi (0.6 ± 0.02 mA/cm^2) (fig. S18C). The enhancement factor is close to the 2.6 times evaluated at 0.9 V versus RHE.

We further evaluated the durability of the surface-modified PtCuNi catalysts and original PtCuNi catalysts by conducting 20,000 cycles of accelerated degradation test (ADT) and performing post-mortem characterizations (figs. S21 to S23). After ADT, the surface-modified PtCuNi catalysts still showed a highly respectable SA and MA of 12.3 mA/cm^2 and 6.6 A/mg_{Pt}, respectively (Fig. 4C and Table 1), exceeding the initial performance of unmodified PtCuNi catalysts, which is also much higher than the as-prepared PtCuNi catalysts after ADT (SA of 5.3 mA/cm^2 and MA of 3.5 A/mg_{Pt}). Despite the similar size after ADT (figs. S22 and S23), the surface-modified PtCuNi catalyst showed ECSA retention of 111%, which is higher than that of the original PtCuNi catalysts (93%). This difference indicates that about 30% of adsorbed DMF was stripped after 20,000 cycles and the remaining DMF still provides considerable activity enhancement. This high number may be associated with partial stripping of the surface-adsorbed molecules (DMF) during

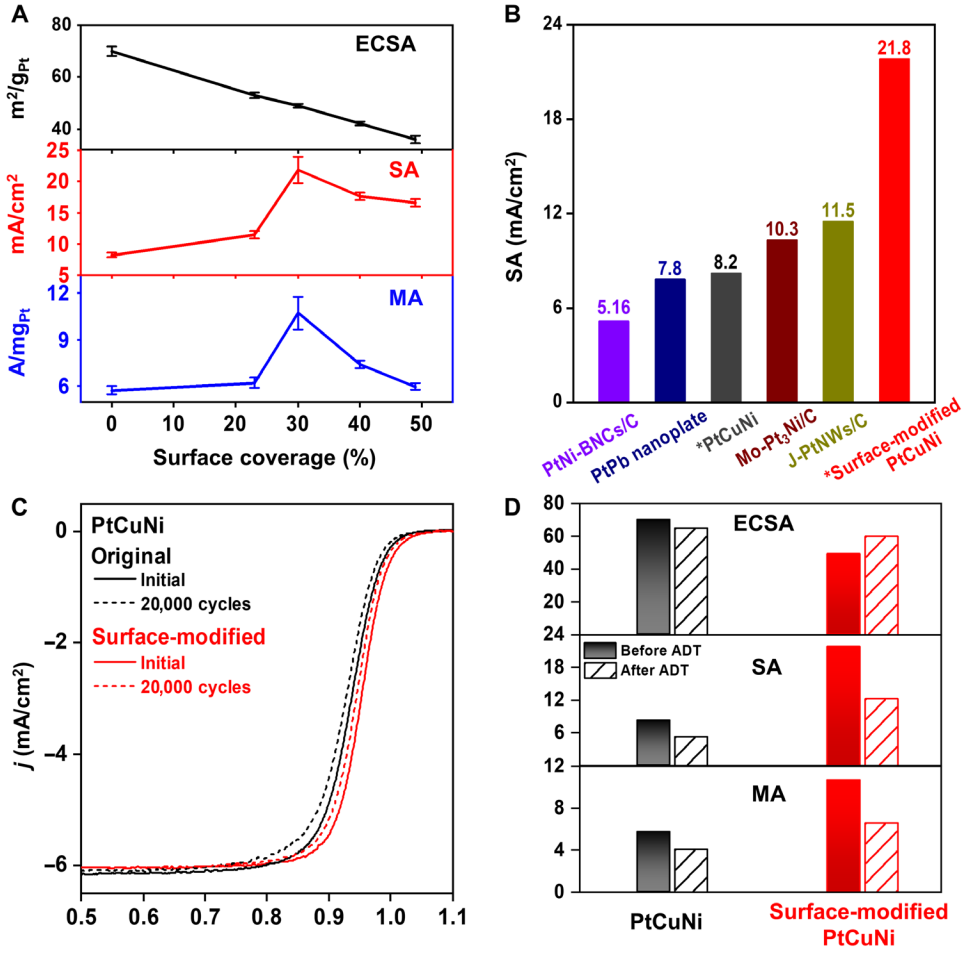

Fig. 4. Performance of PtCuNi catalysts with and without DMF. (**A**) The evolution of ECSA (black), SA (red), and MA (blue) with DMF surface coverage at 0.9 V versus RHE. (**B**) Comparison of SA for optimal surface-modified PtCuNi catalysts and state-of-the-art ORR catalysts. References: PtNi-BNCs/C (*50*), PtPt nanoplate (*51*), Mo-Pt_3Ni/C (*52*), and J-PtNWs (*27*). *PtCuNi and *Surface-modified PtCuNi catalysts are from this work. (**C**) ORR stability LSV curves for original PtCuNi catalysts (black) and optimal surface-modified PtCuNi catalysts (red) before (black solid line and red solid line) and after (black dashed line and red dashed line) 20,000 cycles. (**D**) ECSA, SA, and MA comparisons of PtCuNi catalysts and surface-modified PtCuNi catalysts before and after ADT.

Table 1. RDE performance of surface-modified PtCuNi catalysts in comparison to those in several representative reports. The row in boldface shows the to-date highest reported specific activity and mass activities, along with the electrochemical active surface area and ADT cycles. BOL, the beginning of life; ADT, accelerated degradation test; NA, not available.

Catalyst	SA (mA/cm^2)		MA (A/mg$_{Pt}$)		ECSA (m^2/g$_{Pt}$)	ADT cycles
	BOL	ADT	BOL	ADT		
Surface-modified PtCuNi (this work)	**21.8**	**12.3**	**10.7**	**6.6**	**49**	**20,000**
As-prepared PtCuNi (this work)	8.2	5.3	5.7	3.5	70	20,000
Pt_3Ni nanoframe (*53*)	8.4*	NA	5.7	NA	67.2	10,000
PtNi-BNCs/C (*50*)	5.16	5.15*	3.52	3.47	68.2	50,000
fct-Pt-Co@Pt octahedron (*54*)	9.16	7.21	2.82	2.23	30.8	30,000
PtPb nanoplate (*51*)	7.8	7.0	4.3	3.97	55.0	50,000
PtNi/Ni–B/C (*55*)	9.05	NA	5.3	NA	59	5000
J-PtNWs (*27*)	11.5	10.9*	13.6	12.0	118	6000

*Calculated from the literature.

long-term ADT cycling, exposing more available Pt sites. At the beginning of the reaction, the introduction of the surface molecular pump sacrifices ECSA while boosting SA (or turnover frequency per site) to achieve a high MA. With the progress of the reaction, while the SA of the catalyst decreases with stripped ligands, its ECSA recovers to maintain a decent MA after ADT. This suggests that the surface-modified catalysts can not only show improved catalytic activity but also retain a higher activity after ADT compared to the unmodified ones. Using nuclear magnetic resonance (NMR), we did not find the existence of DMF molecule in electrolyte before and after stability test (fig. S24), which indicated that DMF surface modification is unlikely to poison the electrolyte. Therefore, applying this surface modification approach to the same ORR catalyst enables high activity operation for a longer period. This molecular pump concept is broadly applicable. We found that the surface-modified Pt/C also showed 2.5 times enhanced hydrogen oxidation reaction (HOR) SA and noticeable enhanced MA (fig. S25), which suggested that modified surface can facilitate the mass transport for HOR, where hydrogen gas is pumped to Pt surface and water as the product is quickly removed.

DISCUSSION

To further demonstrate the practical applicability of the proposed surface modification strategy, we performed ORR activity and stability measurements at 65°C. At 65°C, the surface-modified Pt/C exhibited an SA of 2.00 mA/cm^2 and an MA of 0.37 A/mg, which are much higher than those of unmodified Pt/C (an SA of 0.57 mA/cm^2 and an MA of 0.26 A/mg) (fig. S26). The MA of modified Pt/C only decreased by 8.1% after ADT, while the MA of unmodified Pt/C decreased by 42.3% (fig. S26C). The after-ADT MA of modified Pt/C (0.34 A/mg) is still higher than that of unmodified Pt/C (0.26 A/mg). We also found that this surface modification strategy works in MEA (fig. S27). In the MEA test, we found that a commercial surface-modified PtNi showed an MA of 0.64 A/mg at 0.9 V versus RHE, which is higher than that of unmodified PtNi (0.5 A/mg).

In addition, in the practical catalyst system with ionomer, we believe that DMF as a polar hydrophilic aprotic additive at the Pt surface can modulate the surface environments. Two hydrophobic methyl substituents (−CH_3) inhibit interaction with water molecules to disrupt the water network near the Nafion-Pt interface, which facilitates water diffusion and oxygen diffusion. On the other hand, the hydrophilic aldehyde group (−HC═O…) may favor the hydrogen bonding connection with sulfonate groups (…H-O═S) of the Nafion ionomer, stabilizing the adsorbed DMF on the Pt surface. We assume that the paired aldehyde groups and sulfonate groups may reduce the hydrophilicity of the Nafion-Pt interface, further promoting water diffusion and oxygen diffusion.

In summary, we report that surface modification can greatly enhance the ORR activity of Pt-based catalysts by interrupting the surface water adlayer network and hence facilitating the influx of O_2 and outflux of H_2O at the catalyst-electrolyte interface, functioning as a surface molecular pump to promote the rate of the reaction. In particular, combining experimental design and IFF MD simulations provides a quantitative explanation. IFF MD simulations alone reach 10 times higher accuracy than other MD methods to date due to incorporation of deep chemical knowledge into the IFF parameters, full interpretability, and validation. The simulations showed that DMF-modified Pt surfaces lower the O_2 physisorption free energy to larger negative values, enabling better penetration of the interfacial water layer. The result equates to a two- to threefold increase in local O_2 concentration and hence a two- to threefold increase in SA toward ORR, following Le Chatelier's principle. We further showed that this effect can be used independently and in conjunction with the Sabatier principle (strain-ligand effect). Accordingly, we demonstrated a record-high SA of 21.8 ± 2.1 mA/cm^2 (at 0.9 V versus RHE) on DMF-modified PtCuNi catalyst. Unlike current studies that focus on modifying surface hydrophobicity to alter intermediate binding energy or reaction pathways (*37*), our strategy aims to enhance oxygen availability and expedite water removal, thus driving the reaction toward a more efficient ORR process. This study opens an exciting avenue to modulate catalytic activities through designing and constructing local environments at the molecular level that enhance reaction kinetics at the catalyst-electrolyte interfaces. Future studies may also illuminate the role of ionomers for the dynamics of oxygen and hydronium ions at the catalyst surface.

MATERIALS AND METHODS

Chemicals

Platinum(II) acetylacetonate [Pt(acac)$_2$, 97%], nickel(II) acetylacetonate [Ni(acac)$_2$, 95%], copper (II) acetate [Cu(AC)$_2$, 97%], perchloric acid ($HClO_4$, 70%, PPT grade), glucose, oleylamine [OAm; $CH_3(CH_2)_7CH{=}CH(CH_2)_7CH_2NH_2$, >70%], 1-octadecene [ODE; $CH_2{=}CH(CH_2)_{15}CH_3$; technical grade, >90%], and 5 wt % Nafion were all purchased from Sigma-Aldrich. Commercial Pt/C catalyst (40 wt % Pt) was purchased from Alfa Aesar. DMF (≥99.8%), ethanol (200 proof), and cyclohexane (C_6H_{12}; analytical reagent, >99.5%) were obtained from EMD Millipore and Decon. Isopropanol (≥99.5%) was purchased from Thermo Fisher Scientific. All reagents were used as received without further purification. Carbon black (Vulcan XC-72) was received from Carbot Corporation and annealed in 200°C air before used. The deionized water (18 megohm cm) was obtained from an ultrapure purification system (Milli-Q advantage A10). Ultrahigh-purity CO was purchased from Airgas Inc.

Preparation of PtCuNi catalysts

The synthesis of PtCuNi catalysts is similar to a previous report (*36*). In a typical preparation of PtCuNi catalysts, Pt(acac)$_2$ (20 mg), Cu(AC)$_2$ (6 mg), Ni(acac)$_2$ (6 mg), glucose (135 mg), OAm (3 ml), and ODE (2 ml) were added into a vial (volume, 35 ml). The mixture was ultrasonicated for 1 hour and then purged with ultrahigh-purity carbon monoxide (CO) for 5 min and heated from room temperature to 170°C and kept for 12 hours in an oil bath. The colloidal products were collected by centrifugation and washed with cyclohexane/ethanol (v/v = 1:5) mixture two times. The PtCuNi catalysts were then loaded onto 20 mg of carbon black (Vulcan XC-72) by sonication for 2 hours. The as-prepared PtCuNi catalysts were suspended in 20 ml of cyclohexane/ethanol (v/v = 1:1) mixture. To load the sample onto carbon black, 20 mg of carbon black was added and sonicated for 2 hours. The resulting catalysts were collected by centrifugation, washed with cyclohexane/ethanol mixture, and annealed at 130°C for 6 hours in a homebuilt tube furnace with an Ar flow of 100 standard cubic centimeters per minute.

Application of surface-modified PtCuNi catalyst and Pt/C catalyst

The resulting dried PtCuNi catalysts or as-received Pt/C catalysts were first dispersed in DMF with a concentration of 1 mg/ml and ultrasonicated for 20 min. The resulting solution was heated with magnetic stirring in an oil bath at 120°C for the desired time to absorb DMF. After the modification, the resulting catalysts were washed with IPA three times and further dried in a vacuum dryer.

Structure and composition characterization

High-resolution transmission electron microscope (HRTEM) images, energy-dispersive x-ray spectroscopy (EDX) line-scan file, and the high-angle annular dark-field scanning transmission electron microscope (HAADF-STEM) images were taken on a JEM-ARM300F Grand ARM Transmission Electron Microscope operated at 300 kV. TEM samples were prepared by dropping ethanol dispersion of catalysts onto carbon-coated aluminum TEM grids (Ted Pella, Redding, CA). The Pt loading of catalysts was determined by the inductively coupled plasma atomic emission spectroscopy. The Pt loading is determined before electrochemical measurement. XPS tests were carried out on a Kratos AXIS Ultra DLD spectrometer. All samples were electrochemically activated before XPS tests. The NMR measurement was performed on a Bruker AV400 NMR Spectrometer. 3-(Trimethylsilyl)propionic-2,2,3,3-d4 acid sodium salt was used as the internal standard.

Electrochemical measurements

A three-electrode cell system was used to conduct all electrochemical tests. The working electrode was a glassy carbon rotating disk electrode (RDE) with a 0.196 cm^2 glassy carbon geometry area from Pine Instruments. The counter and reference electrodes are Pt coil and Ag/AgCl (3 M Cl^-). For activity measurement, Pt loadings were 10.2 and 7.85 μg/cm^2 for Pt/C catalysts and all PtCuNi catalysts, respectively. CV activations were performed in N_2-saturated 0.1 M $HClO_4$ electrolyte with a potential scan rate of 100 mV/s. The ECSA determined by H_{upd} was calculated by integrating the hydrogen adsorption charge on the CV curve by taking a value of 210 μC/cm^2 for the adsorption of a hydrogen monolayer. The ORR was measured in an O_2-saturated 0.1 M $HClO_4$ electrolyte with a potential scan rate of 20 mV/s. The measurement temperature was set at 25°C using a water bath five-neck flask. The current density of the ORR polarization curve was iR-corrected during the measurements. The kinetic current was determined by the Koutecký-Levich equation. This kinetic current was then normalized by the ECSA to obtain the SA. The accelerated durability test (ADT) was performed at room temperature in O_2-saturated 0.1 M $HClO_4$ solutions by applying CV sweep between 0.6 and 1.0 V versus RHE at a sweep rate of 100 mV/s for 20,000 cycles. The ORR activity was measured after 20,000 cycles of ADT. The impedance spectra were recorded with an AC amplitude of 10 mV rms by sweeping the frequency from 100 kHz to 1 Hz at 40 points per decade (data collection on logarithmic scale).

Computational protocols

The atomic/molecular models were prepared using the Materials Studio program (*38*) under three-dimensional (3D) periodic boundary conditions, including the Pt(111) surfaces, H_2O molecules (flexible simple point charge, SPC water model), DMF molecules, O_2 molecules, perchlorate anions, and hydronium cations.

The IFF was used for Pt atoms, O_2 molecules, perchlorate anions, the flexible SPC water model, and hydronium cations using the 12-6 Lennard-Jones (LJ) format [same as Chemistry at Harvard Macromolecular Mechanic (CHARMM) and Consistent Valence Force Field (CVFF)], along with CHARMM36 parameters for DMF molecules. IFF uses a classical Hamiltonian and includes exceptionally accurate parameters for inorganic and organic compounds with systematic validation of chemical bonding (polarity), structures, energies, and physical-chemical interpretability (*12*). IFF parameters for FCC metals are thermodynamically consistent LJ parameters that enable the reproduction of lattice parameters (0.1% accuracy), surface energies (3% accuracy), and hydration energies (~5 to 10% accuracy) relative to experiments, surpassing DFT methods by multiples (*11*, *39*–*41*). The IFF parameters for molecular O_2 reproduce the liquid density, vaporization energy (at boiling point and 1 atm), and solvation free energy (298.15 K) within 3% deviation from experimental measurements down to an accuracy of 0.03 kcal/mol (*13*), also one to two orders of magnitude more accurate than other force fields and quantum methods (*42*). Multiple studies have demonstrated that the dynamics at realistic temperatures and surface properties of metals and their interfacial interactions with solvents can be reproduced in about 95% agreement with experimental data, which is a significant improvement over earlier methods and opens up exciting perspectives on molecular engineering of catalysts (*11*, *29*, *40*, *41*, *43*).

To construct models with different levels of DMF surface coverage, initially a Pt(111) slab with six Pt layers (600 Pt atoms) and a box size of 27.744 × 24.027 × 45.000 $Å^3$ was built. The zone above the Pt layers was filled with up to 175 DMF molecules, corresponding to a slab of liquid DMF of approximately 30 Å thickness, excluding water, to correlate with the conditions of surface modification of Pt catalyst in DMF. The simulation temperature was set to 393.15 K (equivalent to 120°C, treatment temperature). MD simulations were carried out in the isothermal-isobaric ensemble (NPT) at a pressure of 1 atm for 8 ns to reach equilibrium, as previously demonstrated for similar systems (*44*, *45*). The equilibrium configurations were used to determine the number of DMF molecules per unit area corresponding to monolayer coverage. For this purpose, using multiple equilibrium configurations, different numbers of DMF molecules near monolayer coverage were placed flat on the Pt surface and the zone above was kept as a vacuum. MD simulations were carried out in the canonical (NVT) ensemble for 8 ns at 298.15 K, the electrochemical measurement temperature. The structure with the highest number of DMF molecules lying flat on the Pt(111) surface was defined as one monolayer coverage and determined to be 20 DMF molecules for the chosen slab, equal to 33.3 Å surface area per DMF molecule. This average value was used to determine the number of DMF molecules needed to represent different surface coverages in follow-on simulations.

Physisorption of O_2 molecules on the pure and DMF-modified Pt(111) surfaces was investigated using models of supersaturated O_2 solutions in contact with the surface that facilitate extensive adsorption-desorption statistics. The models featured a box size of 69.360 × 62.470 × 53.000 $Å^3$ with 3900 Pt atoms (six atomic layers of Pt), 5557 H_2O molecules (flexible SPC model), 100 O_2 molecules (equivalent to 1.0 M concentration), and 10 hydronium ions and perchlorate anions (equivalent to pH 1.0). This concentration of O_2 was still low enough to avoid correlations between neighbor O_2 molecules. Five model systems with different surface coverages by

DMF molecules were built to represent conditions in experiments. The surface coverage in these models was 0.0, 0.1, 0.3, 0.5, and 0.7 with a corresponding number of 0, 13, 39, 65, and 91 DMF molecules for the chosen box size, respectively. Subsequently, the start structures were subjected to a brief energy minimization and to MD simulations to analyze adsorption using the Nanoscale Molecular Dynamics (NAMD) program (*46*). First, simulations were first equilibrated for 1 ns in the NPT ensemble at a pressure of 1 atm, and then continued for 50 ns in the NVT ensemble to sample O_2 contacts, using equilibrium lattice parameters from the NPT period. All simulations involved 3D periodic boundary conditions, a time step of 1 fs, a summation of LJ interactions with a spherical cutoff at 1.2 nm, a summation of electrostatic interaction using the particle mesh ewals (PME) method with a tolerance of 10^{-4} (high accuracy) and temperature of 298.15 K consistent with electrochemical measurement conditions. 3D snapshots were collected every 1 ps to collect abundant data for the physisorption-desorption dynamics of the 100 O_2 molecules on the Pt(111) surfaces with various amounts of DMF (5 million independent data points for each surface coverage).

In the following, we describe the analysis of average physisorption time, interfacial concentration of O_2 and H_2O, hydrogen bonds per water molecule, and free energy profile of O_2 binding to the surface. The equilibrium trajectories of 50 ns duration were analyzed across the time window from 10 to 50 ns for all models, equal to 40,000 snapshots for each system (equal to 4 million data points for 100 O_2 molecules), using self-developed Python code with the MD Analysis package (*47*, *48*). O_2 molecules (or H_2O molecules) at 3.5 Å or less vertical distance from Pt atoms on the surface were categorized to be in an adsorbed state (*26*). For the calculation of the average physisorption time, we only considered the O_2 molecules that were encountered within 3.5 Å distance from the surface Pt atoms (defined as adsorbed O_2 molecules) and excluded those O_2 molecules that had no contact with the surface. The total physisorption time equals the sum of adsorption time of all O_2 molecules within 3.5 Å distance. The average physisorption time was obtained by dividing the total physisorption time by the number of adsorbed O_2 molecules (hereby, trends would not change if minimum physisorption times up to 100 ps were required).

The interfacial concentrations of O_2 and H_2O are crucial for electrochemical reactions and were defined with a slightly larger cutoff of 5 Å above the top atomic layer of the Pt(111) surface, which includes all molecules in the first layer and in the intermediate space to the second molecular layer (but excluding the second molecular layer) (*11*). The interfacial concentration of O_2 and H_2O was defined as the average number of O_2 and H_2O molecules per unit volume within the interfacial layer with an uncertainty equal to the SEM. All simulations were repeated three times and averaged to gain high accuracy and assure reproducibility.

The number of hydrogen bonds per water molecule were counted within the nearest molecular layer of water atop the Pt(111) surface. The maximum are two hydrogen bonds per H_2O molecule, equal to four shared hydrogen bonds, as found in ice or bulk water, with a strength of about 4.7 kcal/mol per hydrogen bond (equal to approximately half the vaporization energy of water). The criterion of identification of a hydrogen bond (H) O—H···O(H_2) in water was a distance of less than 3.5 Å between the two oxygen atoms and an O—H···O angle within 180° ± 30° (*31*). The average number of H-bonds was calculated by dividing the total number of H-bonds by the total number of H_2O molecules in the adlayer, including periodic images across box boundaries.

The profiles of the free energy of O_2 physisorption were obtained by SMD simulation with the large-scale atomic/molecular massively parallel simulator (LAMMPS) program (*49*). We used LAMMPS for SMD calculations because it has better options for SMD and analyzing the results than NAMD. Otherwise, all results from LAMMPS and NAMD are expected to be equal (within the statistical errors) due to using the same IFF energy expression, parameters, and simulation settings (*23*). We carried out SMD simulations using Pt(111) slabs with and without DMF, respectively. The box size was 24.969 × 24.027 × 65.550 $Å^3$, including six atomic layers of Pt atoms at the bottom, with periodic boundary conditions. DMF molecules were placed flatly on the Pt(111) surface at 50% surface coverage in the same manner as previously described. The model system contained 1000 flexible SPC H_2O molecules and only one O_2 molecule. Hydronium ions were not included as they can interact with the O_2 molecule during the pulling process and cause poor sampling. The O_2 molecule was initially placed at least 12 Å away from the Pt(111) surface in the *z* direction. It was coupled via a harmonic spring to a virtual point closer to the surface, which was pulled with a constant velocity toward the Pt(111) surface. The free energy was sampled using a pulling velocity of 1 Å/ns at distances larger than 6 Å. When the O_2 molecule moved closer than ~6 Å to the surface atomic layer of Pt, the pulling velocity of the virtual point was decreased to 0.03 Å/ns for the model with water and 0.01 Å/ns for the model with DMF to ensure better convergence (the accuracy is high and results are identical for any value below a specific critical speed, and above a critical speed the results lose accuracy). Because the DMF molecules are mobile, including hopping and free rotation on the Pt surface, simultaneous rearrangements of the interfacial water networks occur. The given pulling velocities were slow enough to achieve equilibrium sampling of O_2 interactions within the metal-water interfacial region, especially while passing through the immediate water adlayers that have strong interactions with both the metal surface and their neighbor molecules. Using a pulling velocity of 0.01 Å/ns or less then mimics a reversible process and serves to obtain an accurate free energy profile. To avoid movement of the platinum slab, the bottom atomic layer of the slab was constrained in the pulling direction (*z* direction) while allowing mobility in the other directions. In summary, the SMD simulations captured the approach of O_2 molecules from solution to physisorption on the surface for the entire electrode-electrolyte interface including the Pt(111) surface, surface-adsorbed DMF molecules, explicit H_2O molecules, O_2 molecules, and extensive dynamics over a period of 400 ns for each replica (4 μs for all replicas). The simulation models fully consider the hydration of oxygen molecules while traveling from solution to the Pt surface, as well as changes in hydration upon proximity to ions in solution and coordination with DMF on the surface. The distance of the O_2 molecule from the Pt surface was measured between the center of mass of an O_2 molecule and the *z* coordinate of the surface layer Pt atoms.

Specifically, the two model systems for SMD were first pre-equilibrated for 1 ns in the NPT ensemble, and then the SMD protocol was carried out in the NVT ensemble. The trajectory frames and corresponding free energies were collected every 1 ps to generate a high-quality free energy profile. The Visual Molecular Dynamics (VMD) program was used to determine the distance between the center of mass of the O_2 molecule and the Pt(111) surface atomic layer in each frame. The calculated free energies were then plotted versus the distances between O_2 and the Pt (111) surface layer. We

noticed that a slower pulling speed changes the simulated free energies. Below a certain threshold, the results converge to constant free energies, become trustworthy, and allow full sampling of the metal-DMF-water-oxygen interfacial structure. In earlier work (*11*), a faster speed (0.1 Å/ns) was sufficient because Pt surface modification and ions were not present. Convergence could then be reached to compare the adsorption free energies of O_2 on various Pt(hkl) facets. In the current work, the extensive local dynamics of the DMF molecules on the Pt(111) surface and simultaneous rearrangements of the water network required longer simulation times and many repeats to reach convergence of the free energy profiles of O_2. Therefore, we used a pulling speed of 0.01 Å/ns (or slower) at distances <6 Å to favor accuracy over speed. The SMD simulations were repeated with the same settings for over 10 times for better results, about 400 ns simulation time for each replica, and equal to a total simulation time of 4 μs at a DMF coverage of 50%.

For the calculation of the O_2 stabilization energy, we used the Materials Studio graphical user interface (*38*) to cut out representative small molecular clusters from the snapshots of the regular MD trajectories, typically consisting of one O_2 molecule, the surrounding H_2O and DMF molecules, and two atomic layers of Pt atoms below (to provide enough interactions with the adsorbed O_2 molecule). For each composition, two systems, namely, the surface system and the away system, were created with the same number and types of atoms (fig. S13A). For the surface system, the O_2 molecule was typically in contact with the Pt(111) surface, while the O_2 molecule in the away system was at least 20 Å detached from the Pt(111) surface. The calculations used IFF (not DFT, which would be associated with several times higher errors and uncertainties) and the Discover (or Forcite) program in Materials Studio to carry out 200 steps of energy minimization/geometry optimization for each cluster to obtain a physically justified start structure, followed by single-point energy calculations. The spherical cutoff distance of pairwise atom-atom LJ interactions was set to be 12 Å, and the accuracy of the summation of Coulomb interactions was 10^{-5} kcal/mol using the Ewald method. Hereby, Materials Studio and the Discover program are more convenient and faster to create the clusters and conduct energy minimization and single-point energy evaluations than NAMD and LAMMPS. The results are identical among all three programs within statistical simulation errors when the same IFF energy expression and simulations parameters (including cutoff settings) are used (*23*). At least four independent clusters for each DMF content were analyzed in this manner to obtain an average O_2 stabilization energy as well as a standard deviation. The O_2 stabilization energy was calculated using the following equation

$$E_{st} = E_{sur} - E_{away} \quad (1)$$

where E_{st} is the O_2 stabilization energy, E_{sur} represents the total energy of the surface system, and E_{away} is the total energy of the away system (fig. S13A). Typical clusters are displayed in fig. S13B.

To calculate the physisorption energy of DMF on Pt(111), Cu(111), and Ni(111) surfaces, a two-box method was used. The box size was 27.744 × 24.027 × 100.000 $Å^3$ for Pt(111), 28.115 × 22.135 × 100.000 $Å^3$ for Cu(111), and 27.410 × 21.580 × 100.000 $Å^3$ for Ni(111) systems. The first model system was called the desorbed system, where DMF molecules were detached from the metal surface. The second model system was the adsorbed system, where DMF molecules were in contact with the metal surface. All systems included six metal atomic layers, 6480 H_2O molecules, and one DMF molecule. Upon completion of the simulations, the average total energies of the two individual boxes were corrected to the exact target temperature of 298.15 K utilizing the heat capacity of each system, which eliminates potential errors up to 5.0 kcal/mol in adsorption energies. The simulation settings were the same as described above for standard MD over 50 ns. The physisorption energy E_{phys} was calculated using the following equation

$$E_{phys} = E_{ads} - E_{des} \quad (2)$$

where E_{ads} is the average energy of the adsorbed system and E_{des} represents the average energy of the desorbed system.

Supplementary Materials

The PDF file includes:
Figs. S1 to S27
Legend for data S1

Other Supplementary Material for this manuscript includes the following:
Data S1

REFERENCES AND NOTES

1. Z. W. Seh, J. Kibsgaard, C. F. Dickens, I. Chorkendorff, J. K. Nørskov, T. F. Jaramillo, Combining theory and experiment in electrocatalysis: Insights into materials design. *Science* **355**, eaad4998 (2017).
2. P. Strasser, S. Koh, T. Anniyev, J. Greeley, K. More, C. Yu, Z. Liu, S. Kaya, D. Nordlund, H. Ogasawara, M. F. Toney, A. Nilsson, Lattice-strain control of the activity in dealloyed core–shell fuel cell catalysts. *Nat. Chem.* **2**, 454–460 (2010).
3. V. R. Stamenkovic, B. Fowler, B. S. Mun, G. Wang, P. N. Ross, C. A. Lucas, N. M. Marković, Improved oxygen reduction activity on $Pt_3Ni(111)$ via increased surface site availability. *Science* **315**, 493–497 (2007).
4. C. Cui, L. Gan, M. Heggen, S. Rudi, P. Strasser, Compositional segregation in shaped Pt alloy nanoparticles and their structural behaviour during electrocatalysis. *Nat. Mater.* **12**, 765–771 (2013).
5. D. Y. Chung, S. W. Jun, G. Yoon, S. G. Kwon, D. Y. Shin, P. Seo, J. M. Yoo, H. Shin, Y.-H. Chung, H. Kim, B. S. Mun, K.-S. Lee, N.-S. Lee, S. J. Yoo, D.-H. Lim, K. Kang, Y.-E. Sung, T. Hyeon, Highly durable and active PtFe nanocatalyst for electrochemical oxygen reduction reaction. *J. Am. Chem. Soc.* **137**, 15478–15485 (2015).
6. J. Li, S. Sharma, X. Liu, Y.-T. Pan, J. S. Spendelow, M. Chi, Y. Jia, P. Zhang, D. A. Cullen, Z. Xi, H. Lin, Z. Yin, B. Shen, M. Muzzio, C. Yu, Y. S. Kim, A. A. Peterson, K. L. More, H. Zhu, S. Sun, Hard-magnet $L1_0$-CoPt nanoparticles advance fuel cell catalysis. *Joule* **3**, 124–135 (2019).
7. B. Han, C. E. Carlton, A. Kongkanand, R. S. Kukreja, B. R. Theobald, L. Gan, R. O'Malley, P. Strasser, F. T. Wagner, Y. Shao-Horn, Record activity and stability of dealloyed bimetallic catalysts for proton exchange membrane fuel cells. *Energ. Environ. Sci.* **8**, 258–266 (2015).
8. M. Escudero-Escribano, P. Malacrida, M. H. Hansen, U. G. Vej-Hansen, A. Velázquez-Palenzuela, V. Tripkovic, J. Schiøtz, J. Rossmeisl, I. E. L. Stephens, I. Chorkendorff, Tuning the activity of Pt alloy electrocatalysts by means of the lanthanide contraction. *Science* **352**, 73–76 (2016).
9. V. Stamenkovic, B. S. Mun, K. J. J. Mayrhofer, P. N. Ross, N. M. Markovic, J. Rossmeisl, J. Greeley, J. K. Nørskov, Changing the activity of electrocatalysts for oxygen reduction by tuning the surface electronic structure. *Angew. Chem. Int. Ed.* **45**, 2897–2901 (2006).
10. W. Xing, M. Yin, Q. Lv, Y. Hu, C. Liu, J. Zhang, in *Rotating Electrode Methods and Oxygen Reduction Electrocatalysts*, W. Xing, G. Yin, J. Zhang, Eds. (Elsevier, 2014), pp. 1–31.
11. S. Wang, E. Zhu, Y. Huang, H. Heinz, Direct correlation of oxygen adsorption on platinum-electrolyte interfaces with the activity in the oxygen reduction reaction. *Sci. Adv.* **7**, eabb1435 (2021).
12. H. Heinz, T. J. Lin, R. K. Mishra, F. S. Emami, Thermodynamically consistent force fields for the assembly of inorganic, organic, and biological nanostructures: The INTERFACE force field. *Langmuir* **29**, 1754–1765 (2013).
13. S. Wang, K. Hou, H. Heinz, Accurate and compatible force fields for molecular oxygen, nitrogen, and hydrogen to simulate gases, electrolytes, and heterogeneous interfaces. *J. Chem. Theory. Comput.* **17**, 5198–5213 (2021).
14. R. Jinnouchi, K. Kudo, K. Kodama, N. Kitano, T. Suzuki, S. Minami, K. Shinozaki, N. Hasegawa, A. Shinohara, The role of oxygen-permeable ionomer for polymer electrolyte fuel cells. *Nat. Commun.* **12**, 4956 (2021).

15. E. Benn, H. Uvegi, J. Erlebacher, Characterization of nanoporous metal-ionic liquid composites for the electrochemical oxygen reduction reaction. *J. Electrochem. Soc.* **162**, H759–H766 (2015).
16. J. Snyder, T. Fujita, M. W. Chen, J. Erlebacher, Oxygen reduction in nanoporous metal–ionic liquid composite electrocatalysts. *Nat. Mater.* **9**, 904–907 (2010).
17. S. Favero, I. E. L. Stephens, M. M. Titirici, Engineering the electrochemical interface of oxygen reduction electrocatalysts with ionic liquids: A review. *Adv. Energy Sustainability Res.* **2**, 2000062 (2021).
18. G. Yang, S. Yu, Z. Kang, Y. Li, G. Bender, B. S. Pivovar, J. B. Green, D. A. Cullen, F.-Y. Zhang, Building electron/proton nanohighways for full utilization of water splitting catalysts. *Adv. Energy Mater.* **10**, 1903871 (2020).
19. Z. Xie, S. Yu, G. Yang, K. Li, L. Ding, W. Wang, D. A. Cullen, H. M. Meyer, S. T. Retterer, Z. Wu, J. Sun, P.-X. Gao, F.-Y. Zhang, Ultrathin platinum nanowire based electrodes for high-efficiency hydrogen generation in practical electrolyzer cells. *Chem. Eng. J.* **410**, 128333 (2021).
20. D. Strmcnik, K. Kodama, D. van der Vliet, J. Greeley, V. R. Stamenkovic, N. M. Marković, The role of non-covalent interactions in electrocatalytic fuel-cell reactions on platinum. *Nat. Chem.* **1**, 466–472 (2009).
21. L. Lu, Z. Wang, S. Zou, Y. Zhou, W. Hong, R. Li, L. Xiao, J. Liu, X.-Q. Gong, J. Fan, Ligand-mediated bifunctional catalysis for enhanced oxygen reduction and methanol oxidation tolerance in fuel cells. *J. Mater. Chem. A* **6**, 18884–18890 (2018).
22. M. Zorko, P. F. B. D. Martins, J. G. Connell, P. P. Lopes, N. M. Markovic, V. R. Stamenkovic, D. Strmcnik, Improved rate for the oxygen reduction reaction in a sulfuric acid electrolyte using a Pt(111) surface modified with melamine. *ACS Appl. Mater. Interfaces* **13**, 3369–3376 (2021).
23. Y. K. Choi, N. R. Kern, S. Kim, K. Kanhaiya, Y. Afshar, S. H. Jeon, S. Jo, B. R. Brooks, J. Lee, E. B. Tadmor, H. Heinz, W. Im, CHARMM-GUI nanomaterial modeler for modeling and simulation of nanomaterial systems. *J. Chem. Theor. Comput.* **18**, 479–493 (2022).
24. T. Kumeda, N. Hoshi, M. Nakamura, Effect of hydrophobic cations on the inhibitors for the oxygen reduction reaction on anions and ionomers adsorbed on single-crystal Pt electrodes. *ACS Appl. Mater. Interfaces* **13**, 15866–15871 (2021).
25. R. Chen, A. B. McAllister, M. Shen, Detection of zwitterion at an electrified liquid-liquid interface: A chemical equilibrium perspective. *J. Electroanal. Chem.* **873**, 114303 (2020).
26. E. Zhu, W. Xue, S. Wang, X. Yan, J. Zhou, Y. Liu, J. Cai, E. Liu, Q. Jia, X. Duan, Y. Li, H. Heinz, Y. Huang, Enhancement of oxygen reduction reaction activity by grain boundaries in platinum nanostructures. *Nano Res.* **13**, 3310–3314 (2020).
27. M. Li, Z. Zhao, T. Cheng, A. Fortunelli, C. Chen, R. Yu, Q. Zhang, L. Gu, B. Merinov, Z. Lin, E. Zhu, T. Yu, Q. Jia, J. Guo, L. Zhang, W. A. Goddard, Y. Huang, X. Duan, Ultrafine jagged platinum nanowires enable ultrahigh mass activity for the oxygen reduction reaction. *Science* **354**, 1414–1419 (2016).
28. T. Fuchigami, S. Inagi, Organic electrosynthesis, in *Fundamentals and Applications of Organic Electrochemistry*, T. Fuchigami, S. Inagi, M. Atobe, Eds. (John Wiley & Sons, 2014), pp. 217–222.
29. L. Ruan, H. Ramezani-Dakhel, C. Y. Chiu, E. Zhu, Y. Li, H. Heinz, Y. Huang, Tailoring molecular specificity toward a crystal facet: A lesson from biorecognition toward Pt{111}. *Nano Lett.* **13**, 840–846 (2013).
30. J. Wang, T. Cheng, A. Q. Fenwick, T. N. Baroud, A. Rosas-Hernández, J. H. Ko, Q. Gan, W. A. Goddard, R. H. Grubbs, Selective CO_2 electrochemical reduction enabled by a tricomponent copolymer modifier on a copper surface. *J. Am. Chem. Soc.* **143**, 2857–2865 (2021).
31. N. Schwierz, C. V. Frost, P. L. Geissler, M. Zacharias, Dynamics of seeded $A\beta_{40}$-fibril growth from atomistic molecular dynamics simulations: Kinetic trapping and reduced water mobility in the locking step. *J. Am. Chem. Soc.* **138**, 527–539 (2016).
32. M. L. Pegis, C. F. Wise, D. J. Martin, J. M. Mayer, Oxygen reduction by homogeneous molecular catalysts and electrocatalysts. *Chem. Rev.* **118**, 2340–2391 (2018).
33. W. A. Herrebout, B. J. Vanderveken, A. Wang, J. R. Durig, Enthalpy difference between conformers of n-Butane and the potential function governing conformational interchange. *J. Phys. Chem.* **99**, 578–585 (1995).
34. Y.-H. Chung, D. Y. Chung, N. Jung, Y.-E. Sung, Tailoring the electronic structure of nanoelectrocatalysts induced by a surface-capping organic molecule for the oxygen reduction reaction. *J. Phys. Chem. Lett.* **4**, 1304–1309 (2013).
35. M. George, G.-R. Zhang, N. Schmitt, K. Brunnengräber, D. J. S. Sandbeck, K. J. J. Mayrhofer, S. Cherevko, B. J. M. Etzold, Effect of ionic liquid modification on the ORR performance and degradation mechanism of trimetallic PtNiMo/C catalysts. *ACS Catal.* **9**, 8682–8692 (2019).
36. J. Huang, Y. Liu, M. Xu, C. Wan, H. Liu, M. Li, Z. Huang, X. Duan, X. Pan, Y. Huang, PtCuNi tetrahedra catalysts with tailored surfaces for efficient alcohol oxidation. *Nano Lett.* **19**, 5431–5436 (2019).
37. C. Xia, S. Back, S. Ringe, K. Jiang, F. Chen, X. Sun, S. Siahrostami, K. Chan, H. Wang, Confined local oxygen gas promotes electrochemical water oxidation to hydrogen peroxide. *Nat. Catal.* **3**, 125–134 (2020).
38. *Materials Studio, v7. 0.200* (Dassault Systèmes, 2013).
39. H. Heinz, R. A. Vaia, B. L. Farmer, R. R. Naik, Accurate simulation of surfaces and interfaces of face-centered cubic metals using 12–6 and 9–6 Lennard-Jones potentials. *J. Phys. Chem. C* **112**, 17281–17290 (2008).
40. I. L. Geada, H. Ramezani-Dakhel, T. Jamil, M. Sulpizi, H. Heinz, Insight into induced charges at metal surfaces and biointerfaces using a polarizable Lennard-Jones potential. *Nat. Commun.* **9**, 716 (2018).
41. C. Zhu, S. E. Hoff, M. Hémadi, H. Heinz, Accurate and ultrafast simulation of molecular recognition and assembly on metal surfaces in four dimensions. *ACS Nano* **17**, 9938–9952 (2023).
42. Y. Wang, P. Verma, X. Jin, D. G. Truhlar, X. He, Revised M06 density functional for main-group and transition-metal chemistry. *Proc. Natl. Acad. Sci. U.S.A.* **115**, 10257–10262 (2018).
43. L. O. Mark, C. Zhu, J. W. Medlin, H. Heinz, Understanding the surface reactivity of ligand-protected metal nanoparticles for biomass upgrading. *ACS Catal.* **10**, 5462–5474 (2020).
44. H. Heinz, B. L. Farmer, R. B. Pandey, J. M. Slocik, S. S. Patnaik, R. Pachter, R. R. Naik, Nature of molecular interactions of peptides with gold, palladium, and Pd-Au bimetal surfaces in aqueous solution. *J. Am. Chem. Soc.* **131**, 9704–9714 (2009).
45. H. Ramezani-Dakhel, L. Y. Ruan, Y. Huang, H. Heinz, Molecular mechanism of specific recognition of cubic Pt nanocrystals by peptides and of the concentration-dependent formation from seed crystals. *Adv. Funct. Mater.* **25**, 1374–1384 (2015).
46. J. C. Phillips, R. Braun, W. Wang, J. Gumbart, E. Tajkhorshid, E. Villa, C. Chipot, R. D. Skeel, L. Kalé, K. Schulten, Scalable molecular dynamics with NAMD. *J. Comput. Chem.* **26**, 1781–1802 (2005).
47. N. Michaud-Agrawal, E. J. Denning, T. B. Woolf, O. Beckstein, MDAnalysis: A toolkit for the analysis of molecular dynamics simulations. *J. Comput. Chem.* **32**, 2319–2327 (2011).
48. R. J. Gowers, M. Linke, J. Barnoud, T. J. E. Reddy, M. N. Melo, S. L. Seyler, D. L. Dotson, J. Domanski, S. Buchoux, I. M. Kenney, O. Beckstein, MDAnalysis: A Python package for the rapid analysis of molecular dynamics simulations, in *Proceedings of the 15th Python in Science Conference* (SciPy, 2016).
49. S. Plimpton, Fast parallel algorithms for short-range molecular dynamics. *J. Comput. Phys.* **117**, 1–19 (1995).
50. X. Tian, X. Zhao, Y.-Q. Su, L. Wang, H. Wang, D. Dang, B. Chi, H. Liu, E. J. M. Hensen, X. W. Lou, B. Y. Xia, Engineering bunched Pt-Ni alloy nanocages for efficient oxygen reduction in practical fuel cells. *Science* **366**, 850–856 (2019).
51. L. Bu, N. Zhang, S. Guo, X. Zhang, J. Li, J. Yao, T. Wu, G. Lu, J.-Y. Ma, D. Su, X. Huang, Biaxially strained PtPb/Pt core/shell nanoplate boosts oxygen reduction catalysis. *Science* **354**, 1410–1414 (2016).
52. X. Huang, Z. Zhao, L. Cao, Y. Chen, E. Zhu, Z. Lin, M. Li, A. Yan, A. Zettl, Y. M. Wang, X. Duan, T. Mueller, Y. Huang, High-performance transition metal–doped Pt_3Ni octahedra for oxygen reduction reaction. *Science* **348**, 1230–1234 (2015).
53. C. Chen, Y. Kang, Z. Huo, Z. Zhu, W. Huang, H. L. Xin, J. D. Snyder, D. Li, J. A. Herron, M. Mavrikakis, M. Chi, K. L. More, Y. Li, N. M. Markovic, G. A. Somorjai, P. Yang, V. R. Stamenkovic, Highly crystalline multimetallic nanoframes with three-dimensional electrocatalytic surfaces. *Science* **343**, 1339–1343 (2014).
54. M. Xie, Z. Lyu, R. Chen, M. Shen, Z. Cao, Y. Xia, Pt–Co@Pt octahedral nanocrystals: Enhancing their activity and durability toward oxygen reduction with an intermetallic core and an ultrathin shell. *J. Am. Chem. Soc.* **143**, 8509–8518 (2021).
55. D. He, L. Zhang, D. He, G. Zhou, Y. Lin, Z. Deng, X. Hong, Y. Wu, C. Chen, Y. Li, Amorphous nickel boride membrane on a platinum–nickel alloy surface for enhanced oxygen reduction reaction. *Nat. Commun.* **7**, 12362 (2016).

Acknowledgments: This work made use of the facilities in the Irvine Materials Research Institute (IMRI) at the University of California Irvine. We also thank Electron Imaging Center of Nanomachines at CNSI for TEM support. The simulation work was supported by the National Science Foundation (DMREF-1623947, DMREF-2323546, OAC 1931587, and CMMI 1940335) and the University of Colorado-Boulder. We acknowledge computing resources at the Summit supercomputer, a joint effort of the University of Colorado Boulder and Colorado State University, which is supported by the National Science Foundation (ACI-1532235 and ACI-1532236), as well as resources at the Argonne Leadership Computing Facility, which is a DoE Office of Science User Facility supported under contract DE-AC02-06CH11357. **Funding:** This work was supported by the US Department of Energy and Office of Naval Research award N000141812155. **Author contributions:** Conceptualization: J.H., H.H., and Y.H. Methodology, investigation, and visualization: J.H., B.P., C.Z., M.X., Y.L., Z.L., J.Z., S.W., H.H., and Y.H. Supervision: H.H. and Y.H. Writing—original draft: J.H., C.Z., B.P., H.H., and Y.H. Writing—review and editing: J.H., C.Z., B.P., X.D., H.H., and Y.H. **Competing interests:** The authors declare that they have no competing interests. **Data and materials availability:** All data needed to evaluate the conclusions in the paper are present in the paper and/or the Supplementary Materials.

Submitted 31 January 2024
Accepted 31 July 2024
Published 6 September 2024
10.1126/sciadv.ado3942